

Thin-Film PZT Lateral Actuators With Extended Stroke

Kenn R. Oldham, *Member, ASME*, Jeffrey S. Pulskamp, Ronald G. Polcawich, *Member, IEEE*, and Madan Dubey

Abstract—Many microelectromechanical system applications require large in-plane actuation forces, with stroke lengths ranging from submicrometer to tens of micrometers in distance. Piezoelectric thin films are capable of generating very large actuation forces, but their motion is not easily directed into lateral displacement in microscale devices. A new piezoelectric thin-film actuator that uses a combination of piezoelectric unimorph beams to generate lateral displacement has been developed. The piezoelectric actuators were fabricated using chemical-solution-derived lead zirconate titanate thin films. These actuators have demonstrated forces greater than 7 mN at displacements of nearly 1 μm , with maximum stroke lengths at 20 V greater than 5 μm in a 500- μm -long by 100- μm -wide actuator. Force and displacement capabilities can be manipulated through simple changes to the actuator design, while actuator nonlinearity can produce dramatic gains in work capacity and stroke length for longer actuators. [2007-0298]

Index Terms—Actuators, lead zirconate titanate (PZT) ceramics, piezoelectric devices, robots.

I. INTRODUCTION

MICROELECTROMECHANICAL systems (MEMS) rely upon a number of actuation technologies to produce mechanical work in miniature devices. Many applications require lateral actuation to displace microstructures within the surface plane of a device, such as closing a microfluidic valve or translating a microrobotic manipulator. Common actuation mechanisms include electrostatic [1]–[3], piezoelectric [4], [5], electromagnetic [6], [7], and thermal actuators [8], [9], which have all found applications in various situations. Bulk piezoelectric materials are very effective at larger length scales, and the development of lateral piezoelectric actuators based on thin-film piezoelectric materials would provide a powerful new actuation technology to MEMS devices.

MEMS lateral microactuation mechanisms have advantages and drawbacks that result from the transduction mechanism utilized. Electrostatic microactuators, particularly comb-finger arrays, require high voltages to produce large forces; parallel-plate gap-closing arrangements generally increase force but have much shorter stroke lengths. Scratch-drive actuators provide even larger forces, but at even smaller stroke lengths,

and with minimum voltage requirements. Thermal actuators can produce very large forces but require large amounts of actuation power. Similarly, electromagnetic actuators consume large amounts of power to produce large forces and can be very difficult to fabricate.

Traditionally, thin-film piezoelectric actuators have been used only for out-of-plane actuation, where piezoelectric compression induces out-of-plane bending in unimorph or bimorph beams [10], [11]. This differs from bulk piezoelectric materials, where lateral actuation is common, providing high-force high-frequency actuation, although with very limited stroke lengths. Microscale applications in disk drives and atomic-force microscopy have already been demonstrated using bulk lateral actuators. Recently, thin-film piezoelectric lateral actuators have been demonstrated [5]. Thin-film lateral actuators are desirable because thin-film deposition and actuator fabrication can potentially be integrated with other microstructures on a single wafer, producing more highly integrated systems. Unfortunately, existing lateral actuators have utilized undesirable methods for increasing piezoelectric actuator stroke length, either in terms of lost work efficiency or in chip area required to leverage the basic actuation stroke.

We have developed a novel thin-film piezoelectric lateral actuator design that produces lateral displacements from combinations of unimorph actuators. These actuators are capable of providing very high forces over low stroke lengths, or extended stroke lengths at reduced force, from equal footprints, depending on the actuator configuration used. By extending actuator stroke length, these actuators can be extremely useful in situations in which the ability to leverage simple piezoelectric contraction is limited by processing or lithography constraints or by the nature of the actuator applications. Sample applications include lateral actuators for driving rotation of microrobotic joints, where small stroke lengths would limit achievable angles, even about a pivot point, and lateral actuators for driving microfluidic valves, in which many actuators are arrayed to produce an appropriate combination of stroke length and actuation force.

This paper is organized as follows. Section II describes the analytical model for piezoelectric lateral actuator motion. Section III describes the fabrication process for building thin-film piezoelectric lateral actuators. Section IV presents experimental measurements of microactuator force and displacement. Section V concludes this paper.

II. THEORY

The lateral lead zirconate titanate (PZT) actuators are unimorph actuators consisting of four segments. Two “bend-down”

Manuscript received December 19, 2007; revised April 19, 2008. First published July 18, 2008; last published August 1, 2008 (projected). Subject Editor E. Obermeier.

K. R. Oldham is with the Department of Mechanical Engineering, University of Michigan, Ann Arbor, MI 48109 USA (e-mail: oldham@umich.edu).

J. S. Pulskamp, R. G. Polcawich, and M. Dubey are with the U.S. Army Research Laboratory, Adelphi Laboratory Center, Adelphi, MD 20783 USA (e-mail: jpulskamp@arl.army.mil; rpolcawich@arl.army.mil; mdubey@arl.army.mil).

Digital Object Identifier 10.1109/JMEMS.2008.927177

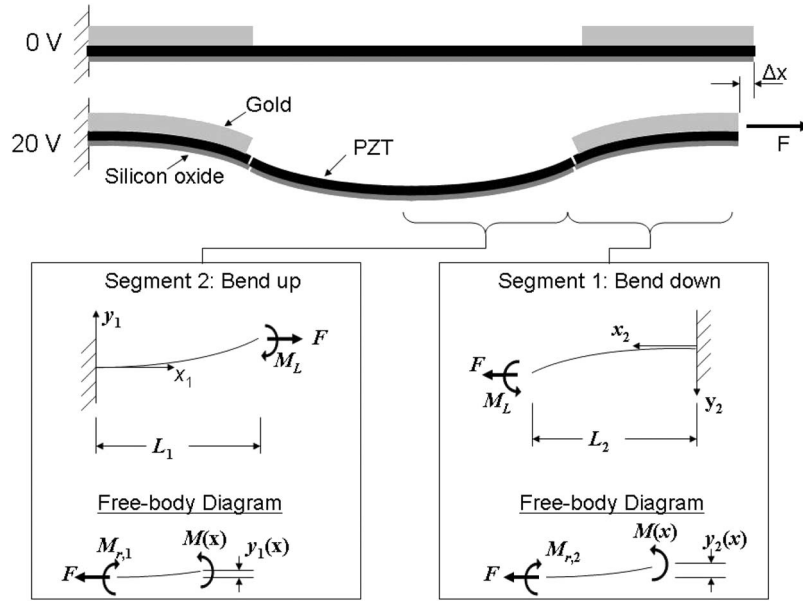


Fig. 1. Schematic diagram of thin-film lateral actuator motion (side views) and free-body diagrams used for analysis.

segments and two “bend-up” segments are located symmetrically on either side of the actuator midpoint, such that net motion at the tip of the actuator is ideally horizontal. In practice, due to residual stresses and process variation, horizontal motion must also be maintained by flexural constraints, which is intended to keep the tip of the actuator moving parallel to the substrate surface. The flexural constraints also guide lateral motion from actuators with mismatched “bend-up” and “bend-down” segments that would deflect out of plane without constraints, which allows greater variation in the design space. The “bend-down” segments use a gold film to move the neutral axis of the unimorph upward to produce the downward bending motion. Gold was selected due to researchers’ previous experience with gold deposition on material stacks incorporating PZT used for microohmic switches [11]; other film materials could potentially be used, with thicknesses being adjusted based on the elastic modulus of the material. The gold-covered segments may be situated either at the ends of the actuator, resulting in downward deflection at the center of the unimorph (as shown in Fig. 1 and tested experimentally), or on the center segments, resulting in upward deflection at the center of the unimorph.

Both the bend-down (segment 1) and bend-up (segment 2) segments of the actuators consist of stacks of silicon dioxide, metal, and PZT thin films, having composite flexural rigidity $(EI)_{\text{comp1}}$ and $(EI)_{\text{comp2}}$ and neutral axes \bar{y}_1 and \bar{y}_2 , respectively. Under an applied voltage V , the PZT film imparts a bending moment M_{act}

$$M_{\text{act}} = e_{31,\text{eff}} \frac{V}{t_{\text{PZT}}} A_{\text{PZT}} (\bar{y}_{\text{PZT}} - \bar{y}_i) \quad (1)$$

where $e_{31,\text{eff}}$ is the effective field-dependent, or electroactive, piezoelectric stress constant of PZT; t_{PZT} is the PZT thickness; A_{PZT} is the cross-sectional PZT area; and E_{PZT} is the elastic

modulus of PZT. The PZT thin film also imposes a contractive force P_{act} and axial strain ε_x

$$P_{\text{act}} = e_{31,\text{eff}} \frac{V}{t} A_{\text{PZT}} \quad (2)$$

$$\varepsilon_x = \frac{P_{\text{act}}}{\sum_i E_i A_i} \quad (3)$$

where $\sum E_i A_i$ is the summation of cross-sectional areas and elastic moduli products of thin films in the stack.

It is important to recognize that $e_{31,\text{eff}}$, as used in the previous equations, is an effective ratio of stress to electric field rather than the exact linear piezoelectric coefficient of the material. This variable $e_{31,\text{eff}}$ accounts for a number of effects, including mechanisms commonly associated with the term “effective piezoelectric coefficient,” as well as other phenomena observed in high-field operation of a piezoelectric material. For most piezoelectric applications, the axial strain (ε_x) within the piezoelectric layer of a cantilever (zero longitudinal stress σ_3) is described by the effective piezoelectric coefficient $e_{31,\text{eff}}$ that is a result of the elastic coupling between the in-plane stress constant e_{31} , the longitudinal stress constant e_{33} , and elastic constants c_{13}^E and c_{33}^E , which is expressed, as in [13], by

$$e_{31,\text{eff}} = e_{31} - \frac{e_{33} c_{13}^E}{c_{33}^E}. \quad (4)$$

However, the typical operating electric fields within MEMS-scale piezoelectric layers exceed the material’s coercive field, and consequently, an effective electroactive coefficient $e_{31,\text{eff}}$ is useful, which includes nonlinear piezoelectric/ferroelectric and electrostrictive material responses that contribute additional strain and enhance the ratio of strain to field, in addition to the behavior described by (4). The electric fields are also in excess

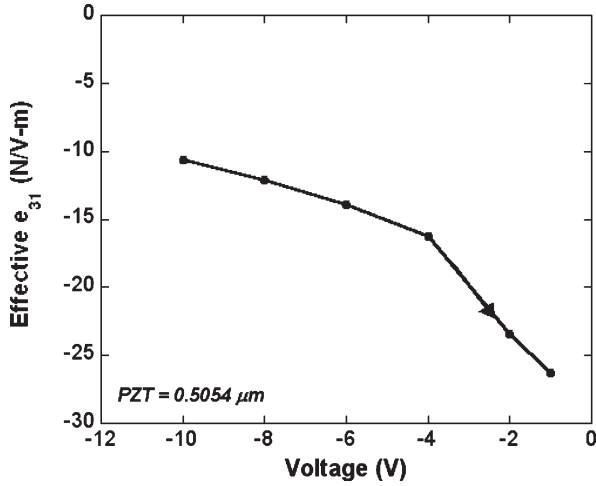


Fig. 2. Effective electroactive stress constant $e_{31,\text{eff}}$ versus voltage for 0.5- μm PZT film.

of the “Rayleigh region” where the properties linearly follow the field and lend themselves to simple analytical models [14].

Due to the lack of models for all phenomena encompassed by the effective electroactive stress constant $e_{31,\text{eff}}$, and the high fields and nonlinearities experienced, values for $e_{31,\text{eff}}$ must be measured experimentally. On each wafer, several cantilever beams of varying lengths are tested to obtain $e_{31,\text{eff}}$ values as a function of voltage, with results being noted for respective experimental results. The magnitude of $e_{31,\text{eff}}$ is extracted from the free out-of-plane deflection of the cantilever test structures, such that the moment calculated from (1) satisfies a small displacement free cantilever deflection profile

$$M = \frac{2(\text{EI})_{\text{comp}} v}{L^2} \quad (5)$$

where v is the vertical deflection of the cantilever tip and L , in this case, is the length of the cantilever beam. A representative plot of $e_{31,\text{eff}}$ is shown in Fig. 2.

Due to symmetry, actuator displacement is calculated using just one side (one of each segment) of the actuator. The bending profiles of the two segments can be found using Euler–Bernoulli beam theory. One end of each segment is assumed to be constrained to in-plane motion by external guides for segment 1 and by symmetry for segment 2. The constraints impart reaction moments $M_{r,1}$ and $M_{r,2}$, and an internal moment M_L may arise where the segments meet. An in-plane load force F is also applied, which imparts a bending moment dependent upon vertical deflection of the segments y_1 and y_2 at position x along the segments. For simplicity, out-of-plane reaction forces are neglected; the amount of force required to keep the actuator in plane is very small, due to its small total thickness, and therefore does not have a large effect on the bending moments. The resulting deflection equations are

$$\frac{M_{\text{act},1} + Fy_1(x) + M_{r,1}}{(\text{EI})_{\text{comp},1}} = \frac{d^2 y_1}{dx^2} \quad (6)$$

$$\frac{M_{\text{act},2} + Fy_2(x) + M_{r,2}}{(\text{EI})_{\text{comp},2}} = \frac{d^2 y_2}{dx^2}. \quad (7)$$

For boundary conditions, the slope at the constrained endpoints is set to zero, while where segments meet, they must have equal slope

$$\left. \frac{dy_1}{dx} \right|_{L_1} = \left. \frac{dy_2}{dx} \right|_{L_2} \quad (8)$$

where L_1 and L_2 are the lengths of two segments.

To keep forces and moments balanced, $M_{r,1}$, $M_{r,2}$, and M_L are calculated as

$$M_{r,1} = -M_L - Fy_1(L_1) \quad (9)$$

$$M_{r,2} = M_L - Fy_2(L_2) \quad (10)$$

$$M_{r,1} + M_{r,2} = -F(y_1(L_1) + y_2(L_2)). \quad (11)$$

The general solution to the previous deflection equations is of the form

$$y_i(x) = \frac{M_{\text{act},i} + M_{r,i}}{F} \left[\cosh \left(\sqrt{\frac{F}{(\text{EI})_{\text{comp},i}}} x \right) - 1 \right]. \quad (12)$$

Solving for the reaction moments using the earlier boundary conditions gives

$$M_{r,2} = \frac{M_{\text{act},1} - M_{\text{act},2} \left(C_1 \frac{S_2}{S_1} + \frac{S_2}{S_1} + C_2 \right)}{1 + \frac{S_2}{S_1} + C_1 \frac{S_2}{S_1} + C_2} \quad (13)$$

$$M_{r,1} = M_{r,2} \frac{S_2}{S_1} + M_{\text{act},2} \frac{S_2}{S_1} - M_{\text{act},1} \quad (14)$$

where C_i and S_i are defined as

$$C_i = \cosh \left(\sqrt{\frac{F}{(\text{EI})_{\text{comp},i}}} L_i \right) - 1 \quad (15)$$

$$S_i = \frac{1}{\sqrt{F(\text{EI})_{\text{comp},i}}} \sinh \left(\sqrt{\frac{F}{(\text{EI})_{\text{comp},i}}} L_i \right). \quad (16)$$

To solve for displacement at the tip of the actuator, the arc length of each segment is numerically integrated to find the x -axis position L_{xi} satisfying

$$\int_0^{L_{xi}} \sqrt{1 - \left(\frac{dy_i}{dx_i} \right)^2} dx_i = L_i^* \quad (17)$$

where L_i^* is the length of the segment under axial strain from the PZT and resisting force

$$L_i^* = L_i \left(1 - \varepsilon_{x,i} + \frac{F}{\sum_i E_i A_i} \right). \quad (18)$$

Total displacement of the actuator tip becomes

$$\Delta x_{\text{act}} = 2(L_1 - L_{x1}) + 2(L_2 - L_{x2}). \quad (19)$$

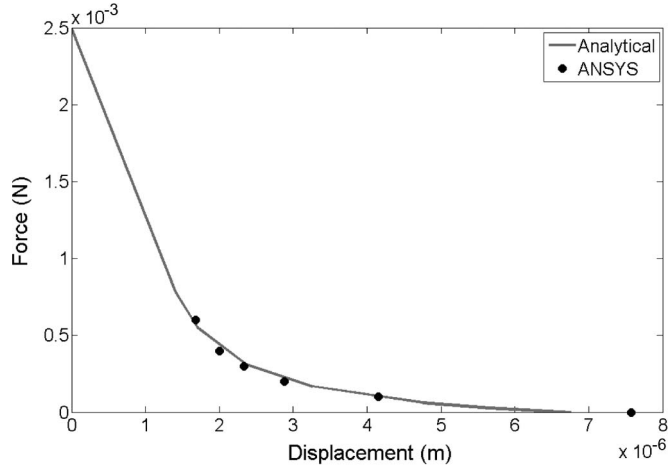


Fig. 3. Analytical force–displacement curve for 500- μm by 100- μm thin-film lateral actuator at 20 V, with 0.12- μm -thick silicon dioxide bottom layer, 0.07- μm platinum electrodes, 0.5- μm PZT thin film, and 1.0- μm gold pads. Gold coverage of 50%, with $e_{31,\text{eff}} = -10.8 \text{ N/m/V}$.

Fig. 3 shows a sample force–displacement curve for a 500- μm -long and 100- μm -wide actuator at 20 V, compared to finite-element analysis simulations. When the opposing force is large, displacements are small, with pure contraction dominating tip displacement. This leads to a linear response similar to a bulk piezoelectric actuator. However, when the opposing force is small, bending of the actuator can significantly increase stroke length, which is greater than 7 μm in the example shown. The primary benefit of increasing stroke length of the actuator is to eliminate the need to leverage small actuator displacements into larger motions. This is useful in cases where an actuator cannot be placed arbitrarily close to the pivot point of a lever arm due to lithography or space constraints.

Several other interesting nonlinearities influence actuator behavior. While out-of-plane displacement increases linearly with the actuator bending moment, in-plane tip displacement, which depends on arc length integrated from the out-of-plane displacements, increases much more rapidly at a roughly quadratic rate. This means that variation in the piezoelectric coefficient has a dramatic effect on actuator performance. Meanwhile, changing the percentage of the actuator in bend-down mode (gold covered) can dictate whether a given design is more applicable to high-force or long-stroke applications, as will be discussed in Section IV.

Increasing actuator length also improves actuator performance. For instance, in microrobotic applications, it can be useful to evaluate actuators based on a work product of force and displacement at various stroke lengths, which can be leveraged in rotation motion with a lever arm [12]. Fig. 4 shows the force–displacement product for actuators ranging in length from 500 to 2000 μm . While the peak levels of work are linearly proportional to actuator length, at specific stroke lengths, available work can improve much more strongly with actuator length. For instance, if a target tip displacement of 2 μm was required, a 2000- μm actuator could do almost four times as much work during one stroke as a 1000- μm actuator could.

The total work W_{TOT} done by the PZT thin film to move the actuator can be written as the sum of the work used to bend

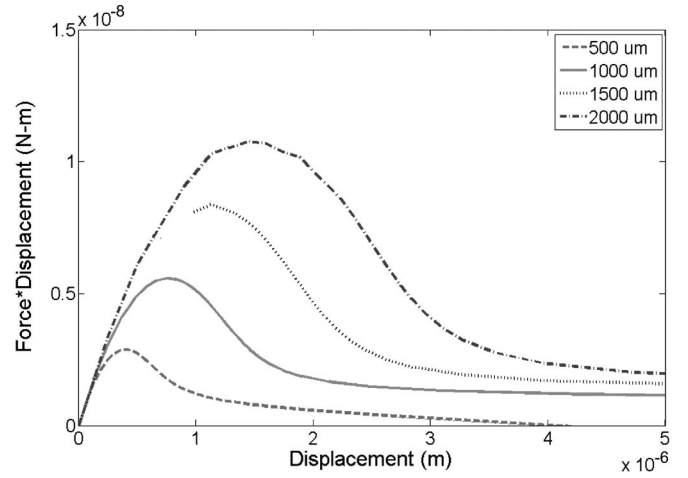


Fig. 4. Force–displacement product (work done against a constant force) versus stroke position for 100- μm -wide actuators of various lengths at 20 V. Gold coverage of 50%, with $e_{31,\text{eff}} = -12.6 \text{ N/m/V}$.

the actuator W_M , to contract the actuator W_P , and to move the external load W_F

$$W_{\text{TOT}} = W_M + W_P + W_F \quad (20)$$

where estimates of these work quantities from angle of deflection and displacement at the tip of the actuator, assuming a constant load, are given by

$$W_M = 2 \left(M_{\text{act},1} \frac{dy_1}{dx} \Big|_{L_1} + M_{\text{act},1} \frac{dy_2}{dx} \Big|_{L_2} \right) \quad (21)$$

$$W_P = 2(P_{\text{act},1}\varepsilon_{x,1}L_1 + P_{\text{act},2}\varepsilon_{x,2}L_2) \quad (22)$$

$$W_F = F\Delta x_{\text{act}}. \quad (23)$$

For large displacements against small loads, the majority of the work done by the PZT thin film is applied to bending the actuator, whereas at low displacement, where contractive deformation is dominant, a much higher percentage of work done by the thin film is applied to the load. Fig. 5 shows a comparison between total work done by the PZT film within the actuator from Fig. 1 and work done against a load force (force–displacement product), as a function of stroke length utilized. For large displacements, with little load force, less than 1% of the PZT film’s work is done against the load, whereas as much as 40% is directed against the load for stroke lengths of less than 1 μm . It should be noted that the electrical energy stored in the piezoelectric film, acting as a capacitor, is also typically one to two orders of magnitude larger than the work done by the actuator. Their ratio is a function of the piezoelectric material’s quasi-static effective electromechanical coupling factor. Thus, charge recovery techniques for piezoelectric actuators are an important requirement for achieving acceptable power consumption in practical applications.

III. FABRICATION

Prototype thin-film piezoelectric lateral actuators were fabricated on a silicon-on-insulator device wafer with a 10- μm -thick

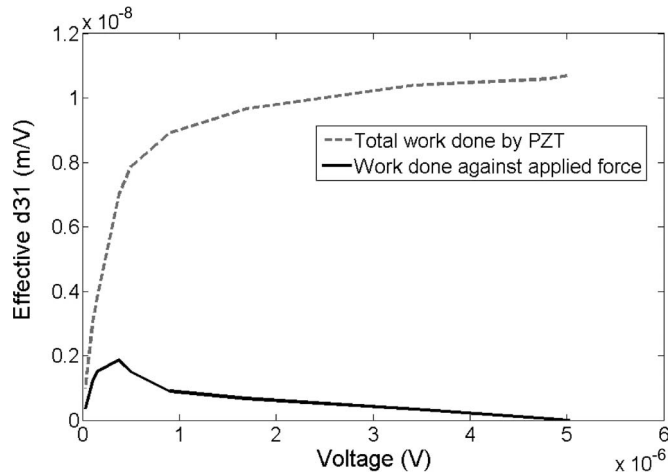


Fig. 5. Total work done by the PZT thin film in the actuator from Fig. 1, and work done against a constant applied load force.

device layer. A silicon dioxide thin film is deposited by plasma-enhanced chemical vapor deposition, followed by a sputtered Ti/Pt bottom electrode for the PZT deposition. The PZT thin films were prepared via a chemical-solution-derived deposition process modified from the one outlined by Budd *et al.* [15]. The silicon oxide layer is necessary to provide proper surface conditions for Ti/Pt and PZT deposition. Chemical solutions were batched with 12% excess lead and were statically dispensed onto the wafer surface. The wafer is then spun at 2500 r/min to thin the solution into a uniform amorphous coating. Afterward, the solution is pyrolyzed at 350 °C to remove most of the volatile organic compounds. This spin and pyrolysis procedure is repeated for a total of four times before the amorphous film is crystallized in PZT using a rapid thermal anneal at 700 °C in flowing oxygen. The actuators outlined in the following work used a PZT thin film with a target thickness of 8000 Å. After the final PZT anneal, a 1050-Å platinum thin film was sputter deposited directly onto the PZT surface at 300 °C; adhesion between Pt and PZT is acceptable without an adhesion layer. See Fig. 6(a) for a schematic of the starting wafer and thin film stack and Table I for a summary of film thicknesses.

The actuator patterning begins with the top platinum and PZT features patterned using two argon ion-milling steps [Fig. 6(b) and (c)], followed by a wet etch to open up contact vias to the bottom electrode [Fig. 6(d)]. A titanium/gold bilayer is deposited via electron beam evaporation on top of the actuators and contact pads and patterned using a liftoff process [Fig. 6(e)]. Trenches are etched through the silicon device layer and buried oxide layer to a depth of 1–2 μm below the buried oxide into the handle wafer [Fig. 6(f)]. Etching below the buried oxide layer allows XeF₂ to etch into the handle wafer, undercutting features formed from the silicon device layers. However, to couple the actuators to silicon microstructures formed from the device layer requires a photoresist encapsulation process prior to actuator release. Silicon features to be preserved are coated in a layer of thick photoresist to protect them from XeF₂. In contrast, the sides of the actuators are not coated to permit XeF₂ to etch the silicon device layer directly beneath the actuator, as well as the handle wafer. Free-moving components must be narrow enough that the XeF₂ etch can undercut the

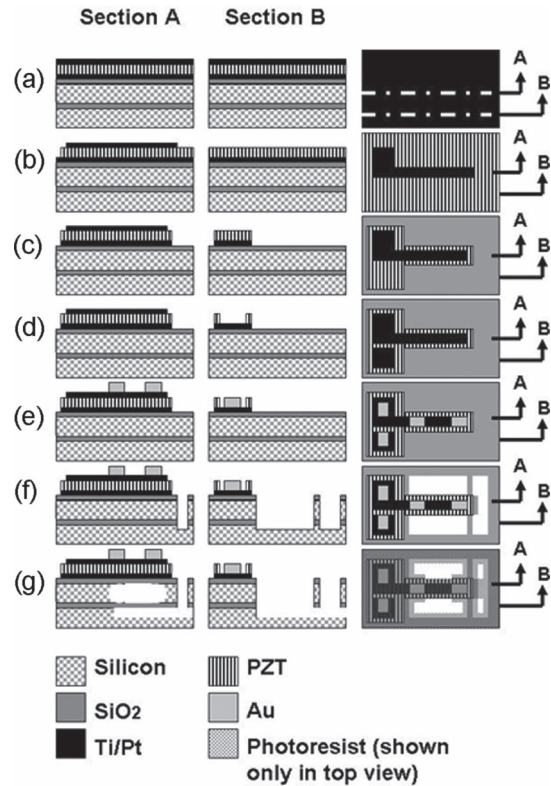


Fig. 6. Process flow for thin-film PZT actuator fabrication. Top view on right; cross-sectional views through lines A and B.

TABLE I
FILM THICKNESSES AND ELASTIC MODULI OF THIN-FILM LATERAL ACTUATOR MATERIALS, EXCEPT WHERE OTHERWISE NOTED

Material	Thickness (μm)	Elastic Modulus (GPa)
Silicon (device layer)	10	170
Silicon Oxide	0.075	80
Platinum (bottom electrode)	0.08	170
PZT	0.8	56
Platinum (top electrode)	0.15	170
Gold	1.0	86

handle layer beneath the protected features in the device layer in a reasonable amount of time [Fig. 6(g)]. After release, there will be buried oxide remaining directly beneath the actuator. This feature cannot be removed directly due to incompatibility between SiO₂ etchants and PZT, but the buried oxide layer is necessary to protect the bottom surface of silicon features during XeF₂ etching. Fortunately, if the oxide layer is thin, it tends to break or buckle and has a minimal effect on actuator motion (see Fig. 7). Last, the photoresist encapsulation layer is removed with an oxygen plasma.

A completed 500-μm-long by 50-μm-wide actuator, which is attached to a silicon/silicon dioxide folded flexure, is shown in Fig. 8. Gold covers the outer quarters of the actuator.

IV. EXPERIMENTAL RESULTS

Microactuator material properties and piezoelectric behavior were characterized prior to microactuator testing. The thicknesses and elastic moduli of the thin films used in the actuator

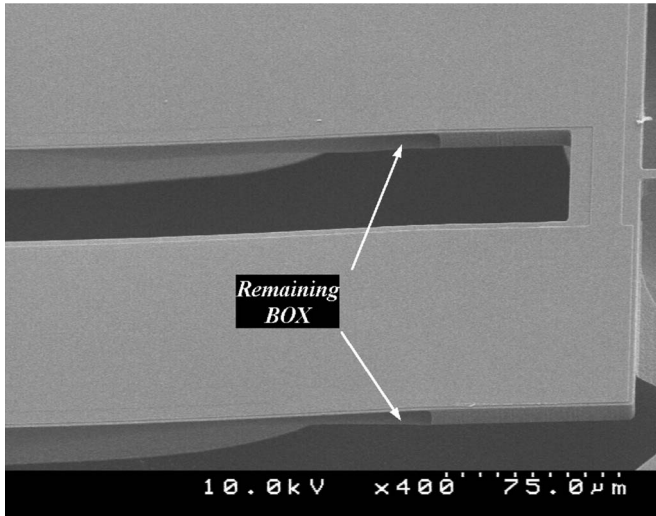


Fig. 7. SEM image of a thin-film lateral actuator, demonstrating compliance in the remaining BOX layer.

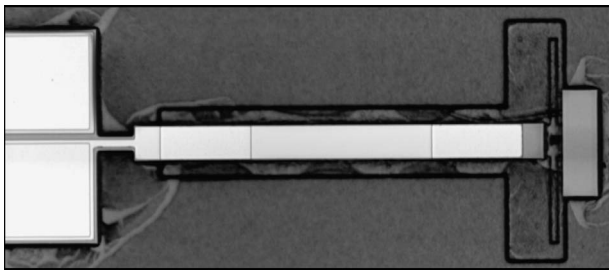


Fig. 8. Thin-film lateral PZT actuator after fabrication prior to release. 500 μm long by 50 μm wide, with 50% gold coverage.

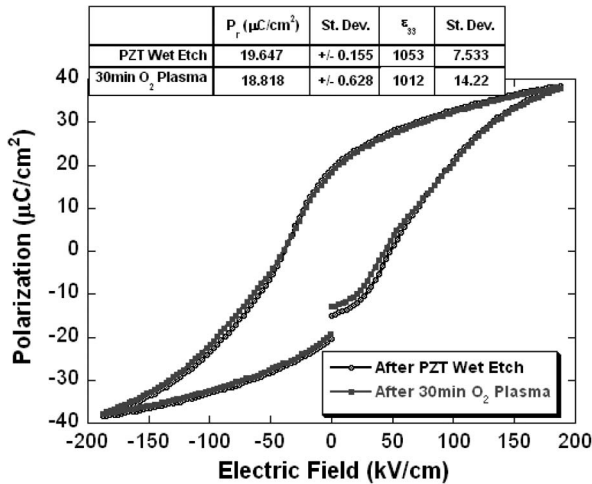


Fig. 9. Representative P - E curve for PZT thin film deposited by chemical solution process.

fabrication process are shown in Table I. The elastic moduli were measured via microtensile testing of the U.S. Army Research Laboratory specimens by Sharpe *et al.* [16], [17]. Ferroelectric properties of the PZT film are monitored throughout the fabrication process, with a sample polarization–electric field P - E curve being shown in Fig. 9 for typical material performance after the PZT wet etch and after a 30-min oxygen plasma. As shown, the average remnant polarization is near 19 $\mu\text{C}/\text{cm}^2$ with a dielectric constant better than 1000. The

effective piezoelectric coefficient $e_{31,\text{eff}}$ is measured from deflection of cantilever beams, as described during the discussion of modeling.

Actuators were fabricated with attachments to three types of force–displacement test structures, as shown in Fig. 10. In each case, the force exerted by the actuator is calculated from displacement or rotation induced in silicon springs, as measured with an optical profilometer. The stiffnesses of these springs were calculated from beam theory. For spring type 1, a folded flexure, force F is calculated from displacement of the actuator tip Δx_{act} as

$$F = \frac{E_{\text{Si}} w_b^3 t_{\text{Si}}}{L_b^3 N_{\text{fold}}} \Delta x_{\text{act}} \tag{24}$$

where w_b and L_b are the width and length of individual folds, E_{Si} and t_{Si} are the elastic modulus and thickness of the silicon device layer, and N_{fold} is the number of folds in the spring.

For spring type 2, a cantilever beam acted on with a perpendicular force, force and displacement are calculated from the rotation angle imparted on a beam $\Delta \theta_{\text{beam}}$

$$F = \frac{E w^3 t}{6 L^2} \Delta \theta_{\text{beam}} \tag{25}$$

$$\Delta x_{\text{act}} = \frac{12 L^3}{E w^3 t} F. \tag{26}$$

For spring type 3, a cantilever beam acted on with parallel force at moment arm of length L_{offset} , force and displacement are again calculated from the rotation angle imparted on a beam

$$F = \frac{E_{\text{Si}} w_b^3 t_{\text{Si}}}{12 L_{\text{offset}} L_b} \Delta \theta_{\text{beam}} \tag{27}$$

$$\Delta x_{\text{act}} = \Delta \theta_{\text{beam}} L_{\text{offset}}. \tag{28}$$

Due to resolution limits on the optical profilometer, rotational angles could be measured much more accurately than displacement at the beam tip, so most measurements shown were obtained from spring types 2 and 3.

Fig. 11 shows the modeled force–displacement curve and experimental data points for a 500- μm -long and 100- μm -wide actuator with 50% gold coverage on the top surface of the actuator (25% of the actuator covered on either end). There is good agreement between the measured data points and expected behavior of the actuator, although there appears to be some variation from actuator to actuator. The actuator was able to apply forces as high as 7 mN at almost 1- μm displacement, and displacements almost to 5 μm , against a 25- μN opposing force. Power dissipation when voltage was applied to the actuators was below the measurement limit of the source meter used during testing, but is predicted to be less than 10 nW for a 100 μm by 500 μm , based on previous measurements of the PZT film resistivity. Thus, the lateral PZT actuators are capable of doing much more work in a given actuator area than typical electrostatic microactuators while consuming much less power than thermal or electromagnetic microactuators.

The percentage of the top surface of the actuator that is coated with gold, and hence “bends down,” has interesting

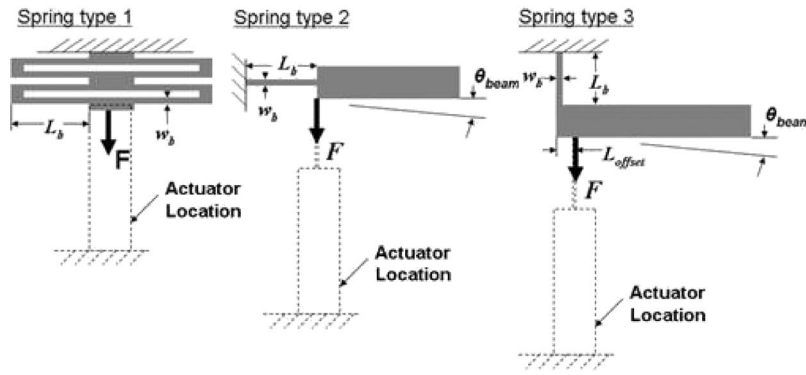


Fig. 10. (Top view) Schematic diagrams of silicon flexure types used to evaluate actuator force and displacement.

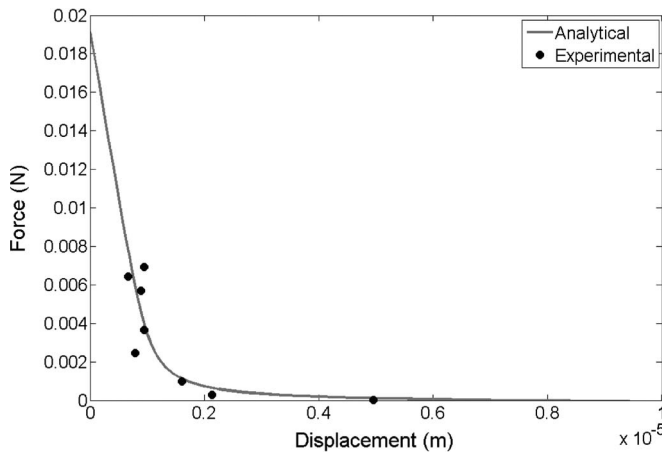


Fig. 11. Comparison of analytical and experimental force–displacement measurements of a 535- μm -long and 100- μm -wide actuator at 20 V, with 50% gold coverage and $e_{31,\text{eff}} = -10.6 \text{ N/m/V}$.

effects on actuator behavior. According to the actuator model, an actuator with two identical platinum electrodes (no silicon dioxide or gold films) would behave like a bulk piezoelectric actuator with simple compression, providing the highest forces from the piezoelectric film. However, it is extremely difficult to build such a perfectly balanced actuator through current processing technology, where a silicon dioxide underlayer is required to prevent platinum silicide formation and differences in thermal budget exist, resulting in upward bending in the actuator to the extent that it is not constrained by guides or flexures. Designing actuators with specified “bend-up” and “bend-down” segments makes this behavior predictable and allows for design optimization. As gold segments are added at the end of the actuator, the sinusoidal shape of the actuator’s profile increases tip displacement, but the additional stiffness of the gold reduces actuation force. Maximum tip displacement increases until about 80% of the actuator is covered with gold, after which further gold coverage is detrimental to performance.

Experimental measurements and analytical models for actuators with 20%, 50%, and 80% gold coverages are shown in Fig. 12, along with the force–displacement curve for the idealized actuator without gold or silicon dioxide films (Pt electrodes only). Both plots show the shift from a shorter stroke and higher force with 20% gold coverage to a longer stroke and lower force actuator with 80% gold coverage. However, experimental

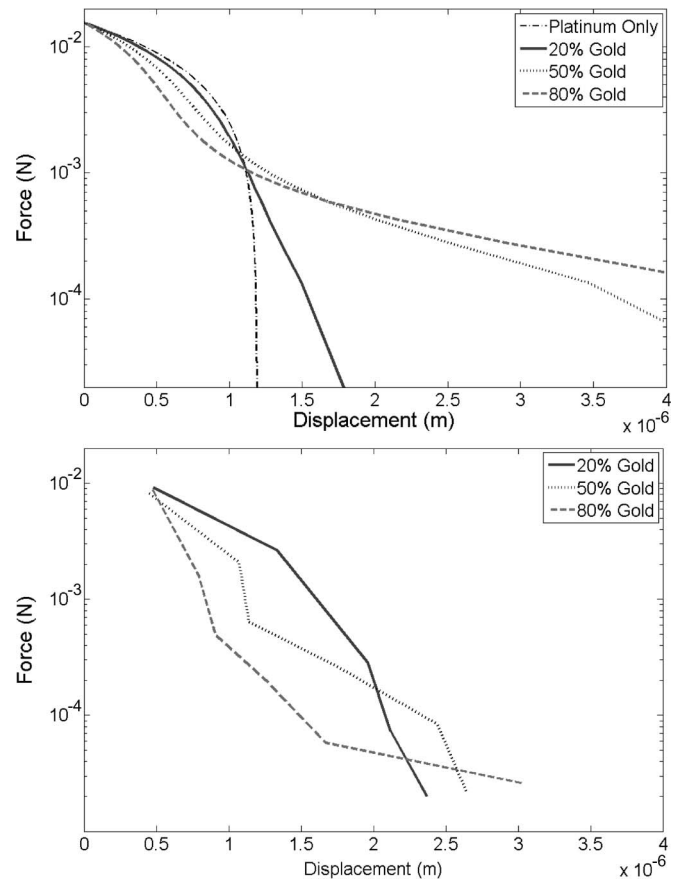


Fig. 12. (Top) Analytical and (bottom) experimental effects of varying percentage gold coverage on thin-film lateral actuators. All actuators are 500 μm long by 100 μm wide at 20 V, with $e_{31,\text{eff}} = -12.6 \text{ N/m/V}$.

actuators with 20% gold outperformed expectations, whereas actuators with 80% gold underperformed. Residual stress in the actuators appears to be the cause of this mismatch; the gold-covered segments of the actuator were found to have residual stresses that were disadvantageous to device operation, whereas segments with silicon dioxide had residual stresses that were slightly advantageous. This can be seen in Fig. 13, where an optical profilometer image of an 80% gold-covered actuator, both before and during actuation, is shown. The gold-covered segments are curled slightly upward after release, canceling out a portion of the actuation moment intended to move the actuator. The opposite is true of the segments without gold,

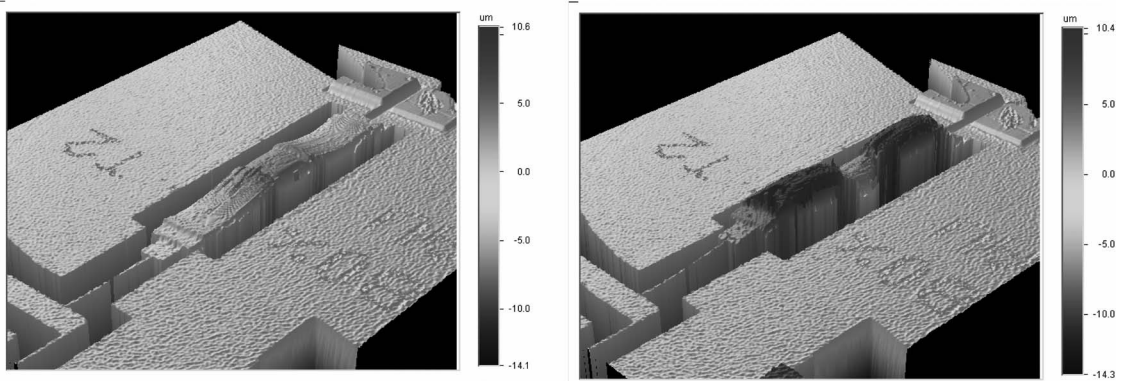


Fig. 13. Optical profilometer images of a thin-film lateral actuator with 80% gold coverage, with (left) 0 V applied and (right) 20 V applied, showing residual stress and curvature of unimorph beam segments with voltage.

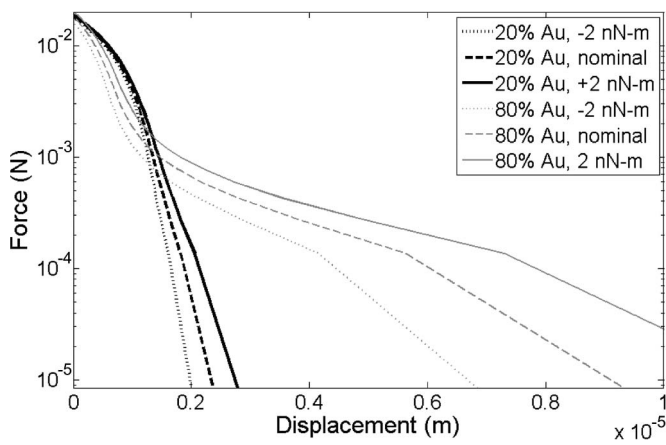


Fig. 14. Simulated effect of a 2-nN · m internal moment generated by residual stress in the gold portion of a 500- μm -long by 100- μm -wide actuator at 20 V, with $e_{31,\text{eff}} = -12.6 \text{ N/m/V}$ and 20% and 80% Au coverages.

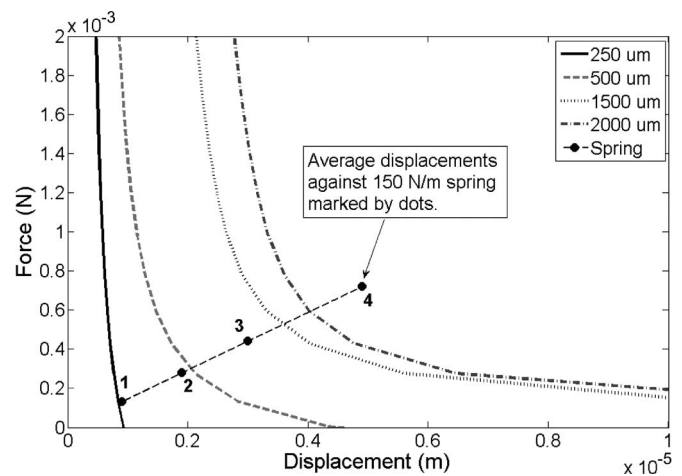


Fig. 15. Analytical force–displacement curves for thin-film actuators of various lengths, compared to displacement measured against a 150-N/m silicon spring. Gold coverage of 50% for all actuators.

which also had a slight upward curl in free cantilever test structures, in this case enhancing actuator motion.

Effects of residual stress can be modeled as an added moment and or force in (1) and (2). Due to the apparent significance of residual stress on actuator results, several scenarios for residual stress were examined. Unfortunately, ability to predict residual stress is limited, except in certain cases [18], and is instead measured experimentally by initial deflection of cantilever beams. While the effects of residual stress depend on residual stresses in both the bend-down (gold-covered) and bend-up (no-gold) portions of the actuator, as well as the percentage of gold coverage, general trends can be shown by Fig. 14 as follows.

- 1) Residual stress contributing to a moment in the direction of desired bending increases tip displacement for a given voltage, whereas residual stress in the opposing direction decreases tip displacement.
- 2) The larger the percentage of the actuator subject to residual stress, the larger the effect.
- 3) Changes in actuator performance are more pronounced in terms of force available for a given displacement than displacement produced against a given load force.

Total actuator length was also examined for actuators ranging from 250 to 2000 μm . Unfortunately, comparative tests

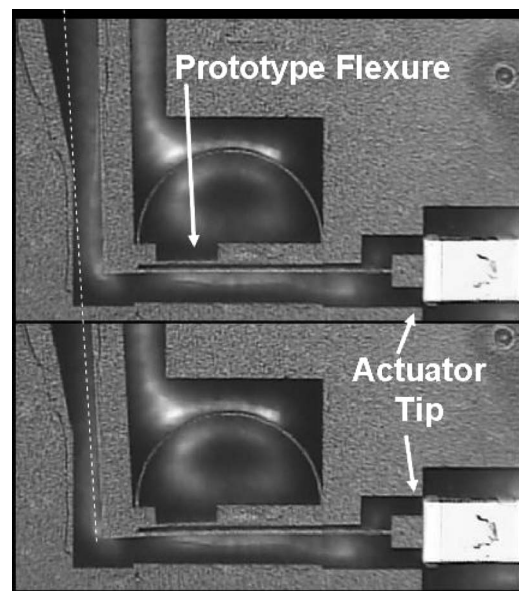


Fig. 16. Prototype rotational flexures for microrobotic applications, operated by a PZT thin-film lateral actuator.

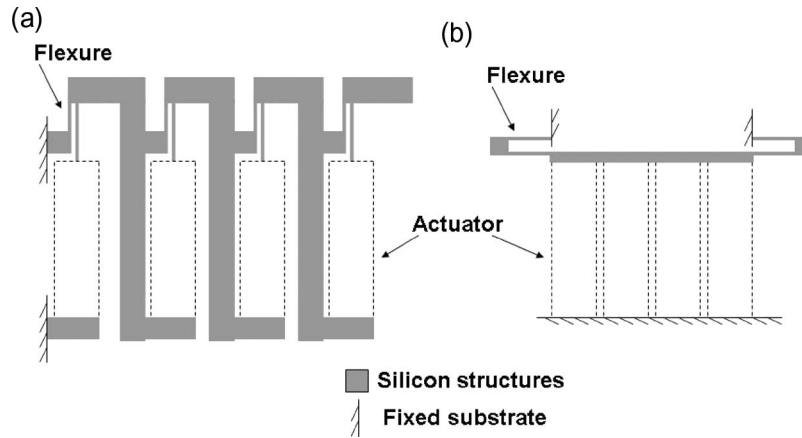


Fig. 17. Schematic top view of multiple (4) actuator arrays to generate (a) series rotational motion and (b) parallel translational motion.

typically varied by as much as a micrometer between measurements, because only test structures of spring type 1 were included on the prototype wafers, and in the case of the longer actuators, optical profilometer resolution was limited by the large field of view required to test the actuators. Fig. 15 shows the analytical force–displacement curves for actuators of four different lengths (250, 500, 1500, and 2000 μm) acting upon a specific spring design for which three samples of each length could be tested. Actuators of 1000 μm were also fabricated but were not released successfully. Measurement accuracy of the 1500- and 2000- μm actuators was only 1 μm , which is insufficient to firmly establish agreement or disagreement between the analytical model and actuator behavior, but the anticipated upward trend in actuator force and displacement was observed.

For many applications, multiple actuators are required to produce desired displacements and/or forces. In these cases, the configuration of the actuators can have a significant effect on whether the excellent work capacity of the actuators alone may be maintained. For instance, to generate the large rotational joint angles desired for microrobotic applications, several actuators and flexures shown in Fig. 16 must be connected in series, as shown schematically in Fig. 17(a). Sets of up to four actuators have been tested experimentally, and designs incorporating eight or more flexures, which are capable of 45° of motion and bearing significant out-of-plane loads, are currently under construction. In a configuration of this type, the connections between actuators approximately double the area required to implement the actuators (not including the flexural area). On the other hand, when actuators are used in series or parallel for purely translational motion, actuators may be placed much more closely together, increasing effective area by only about 25% [Fig. 17(b)]. Likewise, the tethers and flexures used to maintain in-plane motion of the actuator tip when using a single actuator also add to effective actuator area. A typical tether has dimensions of 150 μm by 4 μm and, in the most compact form, is placed parallel with the flexure [as shown in Fig. 17(a)] of about 100 μm by 8 μm . With an adjacent 30 μm of distance required on one side for etch holes, this increases effective actuator area by approximately 15% for a standard 500- μm by 100- μm lateral actuator.

V. CONCLUSION

Thin-film piezoelectric actuators formed from compound unimorph beams have demonstrated extremely high force performance in comparison to other MEMS actuation technologies, with stroke lengths exceeding those of typical piezoelectric materials and maximum forces larger than other common microactuation technologies. Actuators were fabricated from chemical-solution-derived PZT thin films on a silicon-on-insulator wafer and were used to actuate a variety of silicon test structures to evaluate force–displacement performance of a variety of actuator designs. These actuators have potential to serve as an enabling technology for microrobotic manipulators and locomotion, among other applications. Future research will focus on improving actuator robustness and thin-film properties while integrating the lateral actuators with a larger variety of microstructures.

REFERENCES

- [1] W. C. Tang, T. C. H. Nguyen, M. W. Judy, and R. T. Howe, "Electrostatic-comb drive of lateral polysilicon resonators," *Sens. Actuators A, Phys.*, vol. 21–23, pp. 328–331, Feb. 1990.
- [2] T. Imamura, T. Koshikawa, and M. Katayama, "Transverse mode electrostatic microactuator for MEMS-based HDD slider," in *Proc. Int. Workshop MEMS*, 1996, pp. 216–221.
- [3] T. Akiyama and H. Fujita, "A quantitative analysis of scratch drive actuator using buckling motion," in *Proc. IEEE Micro Electro Mech. Syst.*, 1995, pp. 310–313.
- [4] R. B. Evans and J. S. Griesbach, "Piezoelectric microactuator for dual-stage control," *IEEE Trans. Magn.*, vol. 35, no. 2, pp. 977–982, Mar. 1999.
- [5] N. J. Conway and S.-G. Kim, "Large-strain, piezoelectric, in-plane microactuator," in *Proc. 17th IEEE Int. Conf. MEMS*, 2004, pp. 454–457.
- [6] J. S. Han, J. S. Ko, and J. G. Korvink, "Structural optimization of a large-displacement electromagnetic Lorentz force microactuator for optical switching applications," *J. Micromech. Microeng.*, vol. 14, no. 11, pp. 1585–1596, Nov. 2004.
- [7] W. Tang, V. Temesvary, R. Miller, A. Desai, Y.-C. Tai, and D. K. Miu, "Silicon micromachined electromagnetic microactuators for rigid disk drives," *IEEE Trans. Magn.*, vol. 31, no. 6, pp. 2964–2966, Nov. 1995.
- [8] M. J. Sinclair, "A high force low area MEMS thermal actuator," in *Proc. 7th Interc. Conf. Therm. Thermomech. Phenom. Electron. Syst.*, 2000, pp. 127–132.
- [9] C. H. Pan, C.-L. Chang, and Y.-K. Chen, "Design and fabrication of an electro-thermal microactuator with multidirectional in-plane motion," *J. Microlithogr. Microfabr. Microsyst.*, vol. 4, no. 3, pp. 1–15, Jul. 2005.
- [10] Y. Haddab, N. Chaillet, and A. Bourjalt, "A microgripper using smart piezoelectric actuators," in *Proc. Intell. Robots Syst.*, 2000, pp. 659–664.

[11] R. G. Polcawich, J. S. Pulskamp, D. Judy, P. Ranade, S. Trolrier-McKinstry, and M. Dubey, "Surface micromachined microelectromechanical ohmic series switch using thin-film piezoelectric actuators," *IEEE Trans. Microw. Theory Tech.*, vol. 55, no. 12, pp. 2642–2654, Dec. 2007.

[12] K. Oldham, J. S. Pulskamp, R. Polcawich, and M. Dubey, "Thin-film piezoelectric microactuators for bio-inspired micro-robotic applications," presented at the Int. Symp. Integrated Ferroelectrics, Bordeaux, France, 2007.

[13] P. Muralt, A. Kholkin, M. Kohli, and T. Maeder, "Piezoelectric actuation of PZT thin-film diaphragms at static and resonant conditions," *Sens. Actuators A, Phys.*, vol. 53, no. 1, pp. 398–404, May 1996.

[14] D. A. Hall, "Review: Nonlinearity in piezoelectric ceramics," *J. Mater. Sci.*, vol. 36, no. 19, pp. 4575–4601, Oct. 2001.

[15] K. Budd, S. Dey, and D. Payne, "Sol-gel processing of PbTiO₃, PbZrO₃, PZT, and PLZT thin films," *Proc. Brit. Ceramics Soc.*, vol. 36, pp. 107–121, 1985.

[16] W. N. Sharpe, J. Pulskamp, D. S. Gianola, C. Eberi, R. G. Polcawich, and R. J. Thompson, "Strain measurements of silicon dioxide microspecimens by digital imaging processing," *Exp. Mech.*, vol. 47, no. 5, pp. 649–658, Oct. 2007.

[17] K. J. Hemker and W. N. Sharpe, Jr., "Microscale characterization of mechanical properties," *Annu. Rev. Mater. Res.*, vol. 37, pp. 93–126, Feb. 2007.

[18] J. S. Pulskamp, A. Wickenden, R. Polcawich, B. Piekarski, M. Dubey, and G. Smith, "Mitigation of residual film stress deformation in multilayer microelectromechanical systems cantilever devices," *J. Vac. Sci. Technol. B, Microelectron. Process. Phenom.*, vol. 21, no. 6, pp. 2482–2486, Nov. 2003.



Jeffrey S. Pulskamp received the B.S. degree in mechanical engineering from the University of Maryland, College Park, in 2000.

He is currently a Mechanical Engineer with the Micro and Nano Electronic Materials and Devices Branch, U.S. Army Research Laboratory, Adelphi Laboratory Center, Adelphi, MD. His current research interests include RF MEMS devices, electronic scanning antennas, mechanical modeling of MEMS, MEMS actuator design, and millimeter-scale robotics.



Ronald G. Polcawich (M'07) received the B.S. degree in materials science and engineering from Carnegie Mellon University, Pittsburgh, PA, in 1997, and the M.S. (in 1999) and Ph.D. degrees in materials from The Pennsylvania State University, University Park.

He is currently an Engineer and a Team Lead for the RF MEMS Group, Micro and Nano Electronic Materials and Devices Branch, U.S. Army Research Laboratory, Adelphi Laboratory Center, Adelphi, MD. His research interests include RF MEMS devices, electronic scanning antennas, PZT thin films, MEMS fabrication, MEMS actuators, and millimeter-scale robotics.

Dr. Polcawich is a member of the Materials Research Society.



Kenn R. Oldham received the B.S. degree in mechanical engineering from Carnegie Mellon University, Pittsburgh, PA, in 2000, and the Ph.D. degree in mechanical engineering from the University of California, Berkeley, in 2006.

He is currently an Assistant Professor with the Department of Mechanical Engineering, University of Michigan, Ann Arbor. His research interests include microactuation design and application, optimal design and control, and efficient sensing and power circuitry for MEMS devices.

Prof. Oldham is a member of the American Society of Mechanical Engineers.



Madan Dubey received the Ph.D. degree in physics from Banaras Hindu University, Varanasi, India, in 1977.

He is currently a Research Physical Scientist with the Advanced Micro Devices Branch, U.S. Army Research Laboratory, Adelphi Laboratory Center, Adelphi, MD. He is leading a team of researchers in the area of nanoelectronics. He was a Postdoctoral Fellow with North Carolina State University, Raleigh, and was also a Research Engineer with the Research Triangle Institute, Research Triangle

Park, NC.